INTERNATIONAL JOURNAL FOR NUMERICAL METHODS IN FLUIDS
Int. J. Numer. Meth. Fluids 2008; **56**:1765–1786
Published online 23 August 2007 in Wiley InterScience (www.interscience.wiley.com). DOI: 10.1002/fld.1579

Immersed boundary conditions method for unsteady flow problems described by the Laplace operator

S. Z. Husain and J. M. Floryan*, †

Department of Mechanical and Material Engineering, The University of Western Ontario, London, Ont., Canada N6A 5B9

SUMMARY

An implicit, spectral algorithm for the analysis of unsteady flow problems governed by the Laplace operator in corrugated geometries is described. The algorithm treats the physical boundary conditions as constraints along lines internal to the solution domain. The method eliminates the need for coordinate generation and can be quickly adapted to changing geometries. Various tests confirm the spectral accuracy in space and the first- and second-order accuracies in time. Copyright © 2007 John Wiley & Sons, Ltd.

Received 21 November 2006; Revised 21 June 2007; Accepted 22 June 2007

KEY WORDS: immersed boundary conditions method; spectral; partial differential equations; implicit

1. INTRODUCTION

Immersed boundary condition methods involve the use of fixed computational domain with the physical domain of interest submerged inside the computational domain. The name has been coined by Peskin [2] in the context of cardiac mechanics problem. These methods represent a form of meshless methods, where one works with a simple grid system but has to face the challenge associated with the imposition of boundary conditions along the edges of the physical domain. Their advantage lies in the elimination of the costly generation of boundary conforming grid. The physical boundary conditions represent constraints imposed on the field equations, i.e. the problem formulation is closed not by boundary conditions but by a set of constraints.

The prevailing methods of imposition of constraints involve introduction of additional forcing that makes the fluid to move along the physical boundary and thus have roots in the physics of

*Correspondence to: J. M. Floryan, Department of Mechanical and Material Engineering, The University of Western Ontario, London, Ont., Canada N6A 5B9.
†E-mail: mfloryan@eng.uwo.ca

Contract/grant sponsor: SHARCNET
Contract/grant sponsor: NSERC

the problem. The details of the procedures based on the so-called continuous and discrete forcing are reviewed in [1]. Alternative group of methods has its roots in the methodology developed for handling the moving boundary problems and has been reviewed in [3]. Here, the fixed grid methods are of particular interest with the most popular one based on the fluid fluxes and known as the volume of the fluid method. All these methods are of low order in terms of spatial accuracy as they are based on the low-order finite-difference and/or finite-volume discretizations. Additional questions arise in the context of validity and character of the solution of the field equations in the non-physical area located outside the physical domain but inside the computational domain. This issue awaits further investigations.

A formal imposition of internal constraints is described in [4]. This method, which is spectrally accurate, uses representation of flow boundary in the spectral space and imposes constraints by nullifying the relevant Fourier modes. The applicability of this method is limited to geometries that can be represented in terms of Fourier expansions, but its attractiveness is associated with the mathematical formalism and high accuracy. Since this method is particularly suitable for the analysis of flows in rough/corrugated geometries being of interest to us, we focus the present work on the extension of this method to time-dependent situations.

This paper is organized as follows. Section 2 defines the model problem. Section 3 describes the immersed boundary conditions method. Section 4 discusses the domain transformation method. This method uses the classical methodology for the enforcement of boundary conditions and thus provides a good reference point. Section 5 describes results of testing of both the methods. Section 6 compares critically both the methods and Sections 7 provides a summary of the main conclusions.

2. MODEL PROBLEM

Consider unsteady conductive heat flow in a slot bounded by corrugated walls whose geometry is described by the following relations (see Figure 1):

$$y_{\mathrm{L}}(x) = -1 + \sum_{n=-\infty}^{\infty} H_{\mathrm{L}}^{(n)} \, \mathrm{e}^{\mathrm{i}n\alpha x} \tag{1a}$$

$$y_{\mathrm{U}}(x) = 1 + \sum_{n=-\infty}^{\infty} H_{\mathrm{U}}^{(n)} \mathrm{e}^{\mathrm{i}n\alpha x} \tag{1b}$$

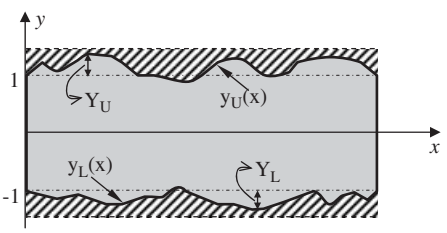

Figure 1. Sketch of the domain of interest in the physical plane.

DOI: 10.1002/fld

where $H_{\mathrm{L}}^{(n)} = H_{\mathrm{L}}^{(-n)*}$, $H_{\mathrm{U}}^{(n)} = H_{\mathrm{U}}^{(-n)*}$ and asterisk denotes complex conjugate. The slot is periodic with wavelength $\lambda = 2\pi/\alpha$ and extends to $\pm\infty$ in the x-direction. The dimensionless field equation describing heat flow has the form

$$\frac{\partial^2\theta}{\partial x^2} + \frac{\partial^2\theta}{\partial y^2} = \frac{\partial\theta}{\partial t} \tag{2}$$

This equation needs to be supplemented by suitable initial and boundary conditions that are taken to be in the form

$$\theta(x, y, t=0) = \theta_i \tag{3}$$

$$\theta(x, y_{\mathrm{L}}(x), t) = C_{\mathrm{L}} = \text{const} \tag{4a}$$

$$\theta(x, y_{\mathrm{U}}(x), t) = C_{\mathrm{U}} = \text{const} \tag{4b}$$

The main difficulty in finding a solution to (2), (3), (4a) and (4b) is associated with the irregular form of the slot. We shall develop two methods, i.e. a method based on the concept of immersed boundary conditions and a method based on the concept of coordinate transformation. The second method is used as a reference method to judge the efficiency and accuracy of the immersed boundary conditions method. We shall begin our discussion with the former method.

3. THE IMMERSED BOUNDARY CONDITIONS METHOD

We are interested in the determination of the solution of (2), (3), (4a) and (4b) with spectral accuracy. We shall use the Fourier expansion in the x-direction and expansion in terms of the Chebyshev polynomials in the y-direction. The standard definition of Chebyshev polynomials uses domain $(-1, 1)$, however, the physical domain is confined between $(1 + Y_{\mathrm{U}})$ and $(-1 - Y_{\mathrm{L}})$, where Y_{U} and Y_{L} denote locations of extremities of the domain of interest (see Figure 1). The first step in the solution process involves a mapping from the physical (x, y) coordinates to the computational $(x, \hat{y})$ coordinates in the form

$$\hat{y} = 2\frac{y - (1 + Y_{\mathrm{U}})}{1 + Y_{\mathrm{U}} - (-1 - Y_{\mathrm{L}})} + 1 \tag{5}$$

where $\hat{y} \in \langle -1, 1\rangle$. The governing equation takes the form

$$\frac{\partial^2\theta}{\partial x^2} + \Gamma^2\frac{\partial^2\theta}{\partial\hat{y}^2} = \frac{\partial\theta}{\partial t} \tag{6}$$

where $\Gamma = 2/(2 + Y_{\mathrm{U}} + Y_{\mathrm{L}})$. The locations of the corrugated boundaries in the $(x, \hat{y})$ plane are given as

$$\hat{y}_{\mathrm{L}}(x) = \sum_{n=-\infty}^{\infty} A_{\mathrm{L}}^{(n)} \mathrm{e}^{\mathrm{i}n\alpha x} \tag{7a}$$

$$\hat{y}_{\mathrm{U}}(x) = \sum_{n=-\infty}^{\infty} A_{\mathrm{U}}^{(n)} \mathrm{e}^{\mathrm{i}n\alpha x} \tag{7b}$$

DOI: 10.1002/fld

where $A_{\mathrm{L}}^{(0)} = 1 + \Gamma[-2 - Y_{\mathrm{U}} + H_{\mathrm{L}}^{(0)}]$, $A_{\mathrm{L}}^{(n)} = \Gamma H_{\mathrm{L}}^{(n)}$ for $n \neq 0$, $A_{\mathrm{U}}^{(0)} = 1 + \Gamma[-Y_{\mathrm{U}} + H_{\mathrm{U}}^{(0)}]$, $A_{\mathrm{U}}^{(n)} = \Gamma H_{\mathrm{U}}^{(n)}$ for $n \neq 0$. The boundary conditions at the transformed boundaries become

$$\theta(x, \hat{y}_{\mathrm{L}}(x), t) = C_{\mathrm{L}} \tag{8a}$$

$$\theta(x, \hat{y}_{\mathrm{U}}(x), t) = C_{\mathrm{U}} \tag{8b}$$

The solution can be represented in the form of Fourier expansion as

$$\theta(x, \hat{y}, t) = \sum_{n=-\infty}^{\infty} \Phi^{(n)}(\hat{y}, t) \mathrm{e}^{\mathrm{i}n\alpha x} \approx \sum_{n=-N_{\mathrm{M}}}^{N_{\mathrm{M}}} \Phi^{(n)}(\hat{y}, t) \mathrm{e}^{\mathrm{i}n\alpha x} \tag{9}$$

where $\Phi^{(n)}(\hat{y}, t) = \Phi^{(-n)*}(\hat{y}, t)$ and asterisk denotes complex conjugate. Substitution of (9) into the field equation and separation of Fourier components lead to an uncoupled system of parabolic partial differential equations for $\Phi^{(n)}$, $n \in \langle 0, N_{\mathrm{M}} \rangle$, of the type

$$\frac{\partial \Phi^{(n)}}{\partial t} = (\Gamma^2 D^2 - n^2 \alpha^2) \Phi^{(n)} \tag{10}$$

where $D = \mathrm{d}/\mathrm{d}\hat{y}$. Two types of temporal discretizations are used. The two-step implicit method results in the following relations:

$$[\Gamma^2 D^2 - (n^2 \alpha^2 + 1.5\Delta t^{-1})] \Phi_{\tau+1}^{(n)} = -2\Delta t^{-1} \Phi_{\tau}^{(n)} + 0.5\Delta t^{-1} \Phi_{\tau-1}^{(n)}, \quad n \in \langle 0, N_{\mathrm{M}} \rangle \tag{11}$$

while similar relations resulting from the one-step, self-starting implicit method are shown in Appendix A. In the above equation, the subscript τ denotes the time step and Δt stands for the (constant) length of the time step. Relation (11) has the form of inhomogeneous ordinary differential equation for $\Phi_{\tau+1}^{(n)}$. The following discussion will be carried out in the context of the two-step method, while the relevant relations for the one-step method can be readily deduced.

The unknown functions $\Phi_{\tau+1}^{(n)}$ can be represented in terms of expansions based on Chebyshev polynomials in the form

$$\Phi_{\tau+1}^{(n)}(\hat{y}) = \sum_{k=0}^{\infty} G_{k,\tau+1}^{(n)} T_k(\hat{y}) \approx \sum_{k=0}^{N_{\mathrm{T}}} G_{k,\tau+1}^{(n)} T_k(\hat{y}) \tag{12}$$

where T_k denotes the Chebyshev polynomial of kth order and $G_{k,\tau+1}^{(n)}$ are the unknown coefficients of the expansion. Substitution of (12) into (11) gives

$$[\Gamma^2 D^2 - (n^2 \alpha^2 + 1.5\Delta t^{-1})] \sum_{k=0}^{\infty} G_{k,\tau+1}^{(n)} T_k = -2\Delta t^{-1} \sum_{k=0}^{\infty} G_{k,\tau}^{(n)} T_k + 0.5\Delta t^{-1} \sum_{k=0}^{\infty} G_{k,\tau-1}^{(n)} T_k \tag{13}$$

We use Galerkin procedure to develop equations for the unknowns $G_{k,\tau+1}^{(n)}$, i.e. we multiply both sides of (13) by $T_j(\hat{y})$ and integrate with the weight function $\hat{\omega} = 1/\sqrt{1 - \hat{y}^2}$ to obtain

$$\sum_{k=0}^{N_{\mathrm{T}}} [\langle T_j, D^2 T_K \rangle - (n^2 \alpha^2 + 1.5\Delta t^{-1}) \langle T_j, T_K \rangle] G_{k,\tau+1}^{(n)}$$

$$= -2\Delta t^{-1} \sum_{k=0}^{N_{\mathrm{T}}} \langle T_j, T_K \rangle G_{k,\tau}^{(n)} + 0.5\Delta t^{-1} \sum_{k=0}^{N_{\mathrm{T}}} \langle T_j, T_K \rangle G_{k,\tau-1}^{(n)}, \quad j \in \langle 0, N_{\mathrm{T}} \rangle \tag{14}$$

DOI: 10.1002/fld

where the inner product is defined as $\langle f_j(\hat{y}), g_k(\hat{y})\rangle = \int_{-1}^{1} f_j(\hat{y}) g_k(\hat{y}) \hat{\omega}(\hat{y})\, \mathrm{d}\hat{y}$. Equation (14) can be simplified by taking advantage of the well-known orthogonality properties, i.e.

$$\langle T_j(\hat{y}), T_K(\hat{y})\rangle = \begin{cases} 0 & \text{for } j \neq k \\ \pi & \text{for } j = k = 0 \\ \pi/2 & \text{for } j = k > 0 \end{cases}$$

Equation (14) leads to $N_\mathrm{T} - 1$ algebraic equations for each Fourier mode; two additional equations required for each Fourier mode in order to close the system need to be derived from the boundary conditions.

The flow boundary conditions are to be enforced along the lines $\hat{y}_\mathrm{L}(x)$ and $\hat{y}_\mathrm{U}(x)$ while the solution domain remains fixed at $\hat{y} \in \langle -1, 1\rangle$. To explain the immersed boundary conditions method in general, we evaluate the unknown $\theta_l(x) \equiv \theta(x, f(x))$ along an arbitrary line, $l := \{(x, y): y = f(x)\}$, such that f is a periodic function with period $\lambda = 2\pi/\alpha$ and $|f(x)| \leqslant 1$. The function $f(x)$ can be expressed without losing generality as

$$f(x) = \sum_{n=-\infty}^{\infty} P^{(n)} \mathrm{e}^{\mathrm{i}n\alpha x} \approx \sum_{n=-N_\mathrm{A}}^{N_\mathrm{A}} P^{(n)} \mathrm{e}^{\mathrm{i}n\alpha x} \tag{15}$$

where one in practice deals with a finite number of terms N_A. The unknown $\theta_l(x)$ is periodic with the same period λ and thus can be expressed in terms of Fourier series as

$$\theta_l(x) \equiv \theta(x, f(x)) = \sum_{n=-N_\theta}^{N_\theta} \varphi^{(n)} \mathrm{e}^{\mathrm{i}n\alpha x} \tag{16}$$

Each modal function is approximated by polynomials up to order N_T and thus the length of this expansion is $N_\theta = N_\mathrm{T} N_\mathrm{A} + N_\mathrm{M}$. Since the flow representation is limited to $N_\mathrm{M} + 1$ modes, we will be able to enforce constraints only on the first $(N_\mathrm{M} + 1)$ terms in (16). The same unknown can be expressed using the discretized form of the solution, i.e.

$$\theta_l(x) = \sum_{n=-N_\mathrm{M}}^{N_\mathrm{M}} \Phi^{(n)}(f(x)) \mathrm{e}^{\mathrm{i}n\alpha x} = \sum_{n=-N_\mathrm{M}}^{N_\mathrm{M}} \sum_{k=0}^{N_\mathrm{T}} G_{k,\tau+1}^{(n)} T_k(f(x)) \mathrm{e}^{\mathrm{i}n\alpha x} \tag{17}$$

Since $T_k(f(x))$ is periodic in x, it can be expressed in terms of Fourier expansion as follows:

$$T_k(f(x)) = \sum_{m=-\infty}^{\infty} w_k^{(m)} \mathrm{e}^{\mathrm{i}m\alpha x} \tag{18}$$

The expansion coefficients in (18) can be evaluated with the help of the recurrence relation for Chebyshev polynomials in the form $T_{k+1}(\hat{y}) = 2\hat{y} T_k(\hat{y}) - T_{k-1}(\hat{y})$ that leads to the following recurrence relation:

$$w_{k+1}^{(m)} = 2 \sum_{n=-\infty}^{\infty} P^{(n)} w_k^{(m-n)} - w_{k-1}^{(m)} \tag{19}$$

whose evaluation begins at $k = 0$ and results in

$$w_0^{(0)} = 1, \quad w_0^{(m)} = 0 \text{ for } |m| \geqslant 1, \quad w_1^{(m)} = P^{(m)} \text{ for } |m| \geqslant 0 \tag{20}$$

DOI: 10.1002/fld

Substitution of (18) into (17) gives

$$\theta_l(x) = \sum_{n=-N_M}^{N_M} \sum_{k=0}^{N_T} \sum_{m=-\infty}^{\infty} G_{k,\tau+1}^{(n)} w_k^{(m)} e^{i(n+m)\alpha x} = \sum_{n=-\infty}^{\infty} \sum_{m=-N_M}^{N_M} \sum_{k=0}^{N_T} G_{k,\tau+1}^{(m)} w_k^{(n-m)} e^{in\alpha x} \quad (21)$$

and comparison of (16) with (21) gives

$$\varphi^{(n)} = \sum_{m=-N_M}^{N_M} \sum_{k=0}^{N_T} G_{k,\tau+1}^{(m)} w_k^{(n-m)} \quad (22)$$

which can be used to express boundary conditions along the lines $\hat{y}_L(x)$ and $\hat{y}_U(x)$. In the case of our model problem, these boundary conditions take the following form:

$$\sum_{m=-N_M}^{N_M} \sum_{k=0}^{N_T} G_{k,\tau+1}^{(m)} (w_U)_k^{(n-m)} = \begin{cases} C_U & \text{for } n=0 \\ 0 & \text{for } n \neq 0 \end{cases} \quad (23a)$$

$$\sum_{m=-N_M}^{N_M} \sum_{k=0}^{N_T} G_{k,\tau+1}^{(m)} (w_L)_k^{(n-m)} = \begin{cases} C_L & \text{for } n=0 \\ 0 & \text{for } n \neq 0 \end{cases} \quad (23b)$$

with (23a) and (23b) corresponding to the upper and lower walls, respectively. Equations (14), (23a) and (23b) form a complete set of algebraic equations for the unknown coefficients $G_{k,\tau+1}^{(n)}$, $k=0,\ldots,N_T$, $n=0,\ldots,N_M$. In the case of a constant time step, the coefficients of the discretized Equations (14) do not depend on time and thus the corresponding matrix of coefficients needs to be inverted only once; the solution process at the subsequent time steps reduces to a simple multiplication of the inverted matrix and the right-hand side of the discretized system. The steady version of the algorithm can be readily developed (description omitted from this presentation). We shall refer to the above method of solution as the 'direct algorithm'.

The matrix of coefficients can be very large when a large number of Fourier modes is required and this motivates search for a method of solution that avoids construction as well as inversion of the complete matrix. The matrix has a structure shown in Figure 2(a) with the horizontal lines showing the coupling effect of boundary conditions (23a) and (23b) and the blocks of coefficients in the upper triangular form resulting from the discretization of the differential equation (10) forming a band along diagonal. The matrix can be reduced to a real form by taking advantage of the complex conjugate properties $\Phi^{(n)}(\hat{y},t) = \Phi^{(-n)*}(\hat{y},t)$ (see Equation (9)) resulting in a very similar structure, as shown in Figure 2(b). Such a structure suggests the use of an iterative solution algorithm based on the decoupling of Fourier modes. The unknowns corresponding to a Fourier mode of interest in Equations (23a) and (23b) at the current time step can be expressed in terms of the remaining Fourier modes using their values from the previous time step (or from the previous iteration). The solution process begins with mode 0, proceeds to the next mode using the most recent information available and continues until the last mode N_M is reached, and then it is repeated until a convergence criterion is satisfied. In this way, the inversion of the complete matrix of size $(N_T+1)*(2N_M+1)$ is replaced by a repetitive solution of system of (N_T+1) equations for each Fourier mode. The rate of convergence is generally very good; it decreases with an increase in the amplitude S and the wavenumber α of the corrugation. We shall refer to the iterative algorithm as the 'decoupled algorithm' and discuss performance of its various variants in Section 6. We wish to stress at this moment that the use of the decoupled algorithm significantly

DOI: 10.1002/fld

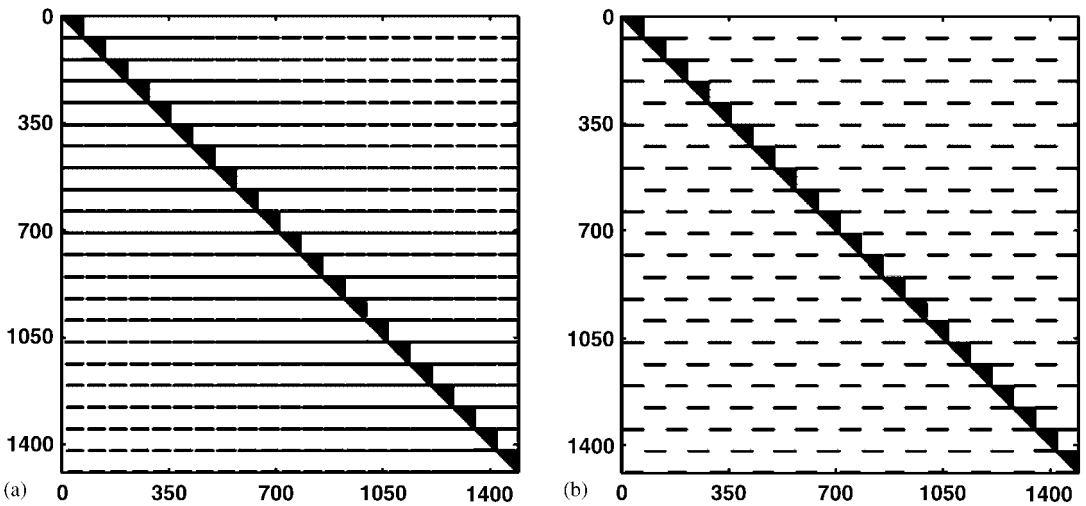

Figure 2. Structure of the coefficient matrix resulting from the implementation of the immersed boundary conditions method for $N_M = 10$ and $N_T = 70$ for the model problem (33). Only non-zero elements are marked. (a) Complex form and (b) real form.

reduces memory requirements as one needs to work with many small matrices rather than the one with very large matrix as well as it opens the possibility for parallelization of the computations. This issue becomes significant in the case of three-dimensional problems and large number of Fourier modes and Chebyshev polynomials.

4. THE DOMAIN TRANSFORMATION METHOD

In this approach, the corrugated slot in the physical domain (x, y) is mapped into a straight slot in the computational domain (ξ, η) using mapping in the form

$$\xi = x, \quad \eta = 2\frac{(y - y_U(x))}{y_U(x) - y_L(x)} + 1 \tag{24}$$

After mapping, Equation (1a) and (1b) take the form

$$\frac{\partial^2\theta}{\partial\eta^2} + W_1(\xi,\eta)\frac{\partial\theta}{\partial\eta} + W_2(\xi,\eta)\frac{\partial^2\theta}{\partial\xi\partial\eta} + W_3(\xi,\eta)\frac{\partial^2\theta}{\partial\xi^2} = W_3(\xi,\eta)\frac{\partial\theta}{\partial t} \tag{25}$$

where $W_1(\xi,\eta) = \eta_{xx}/(\eta_x^2+\eta_y^2)$, $W_2(\xi,\eta) = 2\eta_x/(\eta_x^2+\eta_y^2)$ and $W_3(\xi,\eta) = 1/(\eta_x^2+\eta_y^2)$. Expressions for η_x, η_{xx} and η_y are given in Appendix B. Solution of (25) is represented in terms of Fourier expansion as

$$\theta(\xi,\eta,t) = \sum_{n=-\infty}^{\infty} \Psi^{(n)}(\eta,t)e^{in\alpha\xi} \approx \sum_{n=-N_M}^{N_M} \Psi^{(n)}(\eta,t)e^{in\alpha\xi} \tag{26}$$

DOI: 10.1002/fld

where $\Psi^{(n)} = \Psi^{(-n)*}$ and the known coefficients W_1, W_2 and W_3 are replaced by their Fourier expansions

$$W_1(\xi,\eta) = \sum_{m=-2N_M}^{2N_M} w_1^{(m)}(\eta) e^{im\alpha\xi}, \quad W_2(\xi,\eta) = \sum_{m=-2N_M}^{2N_M} w_2^{(m)}(\eta)\, e^{im\alpha\xi}$$
$$W_3(\xi,\eta) = \sum_{m=-2N_M}^{2N_M} w_3^{(m)}(\eta)\, e^{im\alpha\xi} \tag{27}$$

Substitution of (26) and (27) into (25), separation of Fourier components and the use of a two-step implicit method for the temporal discretization lead to

$$D^2\Psi_{\tau+1}^{(n)} + \sum_{s=-N_M}^{N_M} [w_1^{(n-s)} + is\alpha w_2^{(n-s)}] D\Psi_{\tau+1}^{(s)} - \sum_{s=-N_M}^{N_M} [(s\alpha)^2 + 1.5\Delta t^{-1}] w_3^{(n-s)} \Psi_{\tau+1}^{(s)}$$
$$= -2\Delta t^{-1} \sum_{s=-N_M}^{N_M} w_3^{(n-s)} \Psi_{\tau}^{(s)} + 0.5\Delta t^{-1} \sum_{s=-N_M}^{N_M} w_3^{(n-s)} \Psi_{\tau-1}^{(s)}, \quad n \in \langle 0, N_M \rangle \tag{28}$$

where $D = \mathrm{d}/\mathrm{d}\eta$. A similar expression for the one-step implicit method can be found in Appendix A. The reader may note that all Equations (28) are coupled together through the variable coefficients. The unknown $\Psi_{\tau+1}^{(n)}(\eta)$ can be expressed with spectral accuracy using Chebyshev expansion in the form

$$\Psi_{\tau+1}^{(n)}(\eta) = \sum_{k=0}^{\infty} F_{k,\tau+1}^{(n)} T_k(\eta) \approx \sum_{k=0}^{N_T} F_{k,\tau+1}^{(n)} T_k(\eta) \tag{29}$$

Using the Galerkin procedure described in Section 3 leads to $N_T - 1$ algebraic equations for $F_{k,\tau+1}^{(n)}$ for each Fourier mode. The remaining closing conditions come from the boundary conditions.

The treatment of boundary conditions follows standard procedures. These conditions have the form

$$\theta(\xi, \eta = -1, t) = C_L \tag{30a}$$

$$\theta(\xi, \eta = 1, t) = C_U \tag{30b}$$

Using (26) leads to boundary conditions for each Fourier mode in the form

$$\Psi^{(0)}(-1) = C_L, \quad \Psi^{(n)}(-1) = 0, \quad n \neq 0, \quad \Psi^{(0)}(1) = C_U, \quad \Psi^{(n)}(1) = 0, \quad n \neq 0 \tag{31}$$

Introduction of Chebyshev expansion (29) leads to the required closing conditions in the form

$$\sum_{k=0}^{N_T} (-1)^k F_{k,\tau+1}^{(n)} = \begin{cases} C_L & \text{for } n = 0 \\ 0 & \text{for } n \neq 0 \end{cases} \tag{32a}$$

$$\sum_{k=0}^{N_T} F_{k,\tau+1}^{(n)} = \begin{cases} C_U & \text{for } n = 0 \\ 0 & \text{for } n \neq 0 \end{cases} \tag{32b}$$

DOI: 10.1002/fld

The above process leads to a full matrix of coefficients. In the case of constant timestep simulations, this matrix needs to be inverted only once with the time advancement reduced to multiplication of the inverted matrix with the right-hand side of the discretized equation.

5. TESTING OF THE ALGORITHMS

The following discussion is divided into two parts, with the first one being devoted to the immersed boundary conditions method and the second one being devoted to the domain transformation method. The tests discussed below have been carried out in the context of the following model problem (unless otherwise explicitly noted):

$$y_{\mathrm{L}}(x) = -1, \quad y_{\mathrm{U}}(x) = 1 + (-\tfrac{1}{2}\mathrm{i}S\mathrm{e}^{\mathrm{i}\alpha x} + \mathrm{CC}), \quad \theta_i = 0, \quad C_{\mathrm{L}} = 1, \quad C_{\mathrm{U}} = 0 \tag{33}$$

i.e. the lower wall is smooth, the upper wall has corrugation described by one Fourier mode parameterized by the amplitude S and the wavenumber α, the slot has the initial temperature equal to zero and the temperature of the lower wall is instantaneously raised to 1 at $t = 0$. The term CC in Equation (33) is the abbreviation for 'complex conjugates' and the definition is valid for rest of the manuscript. We are interested in the prediction of the temperature evolution in the interior of the slot and in the distribution of heat flux along the walls as a function of the corrugation amplitude S and the corrugation wavenumber α. The reference, analytical solution of this problem in the case of smooth walls has the form

$$\theta(x, y, t)_{\mathrm{analytical}} = a(y+1) + b + \sum_{m=1}^{\infty} \mathrm{e}^{-(m\pi/2)^2 t} B_m \sin[m\pi(y+1)/2]$$

where $B_m = (m\pi)[(2a+b)\cos(m\pi) - b]/2$, $a = (C_{\mathrm{U}} - C_{\mathrm{L}})/2$ and $b = C_{\mathrm{L}}$.

5.1. Immersed boundary conditions method

As a first step, we wish to demonstrate the spectral accuracy of our algorithm. In the y-direction, the Chebyshev expansions (12) with coefficients calculated using Galerkin procedure (14) are guaranteed to be spectrally accurate with the increasing number of terms N_{T}. In most cases, 60 Chebyshev polynomials provided machine accuracy. This number needs to be increased for $\alpha \to \infty$ (corrugation with shorter wavelength), especially when higher Fourier modes begin to play a role. The need for a larger number of Chebyshev polynomials under such conditions occurs because of the formation of boundary layers around the corrugated wall in the y-distribution of the modal functions $\Phi^{(n)}$. These layers become extremely thin for larger values of α and for higher Fourier modes (see Figure 3). Modal functions change very rapidly inside these layers while they are nearly zero in the rest of the domain. One needs to use a large number of polynomials in order to have sufficient resolution inside the boundary layers and avoid spurious oscillations outside these layers. Typically one needs to use $N_{\mathrm{T}} \approx 80$ for $\alpha = 20$ and $N_{\mathrm{T}} \approx 160$ for $\alpha = 50$.

The second aspect of the spectral accuracy involves the convergence of the truncated Fourier series (9) describing x-variations of the unknown. In all tests dealing with this issue, the number of Chebyshev polynomials N_{T} was kept sufficiently large in order to reduce the associated error

DOI: 10.1002/fld

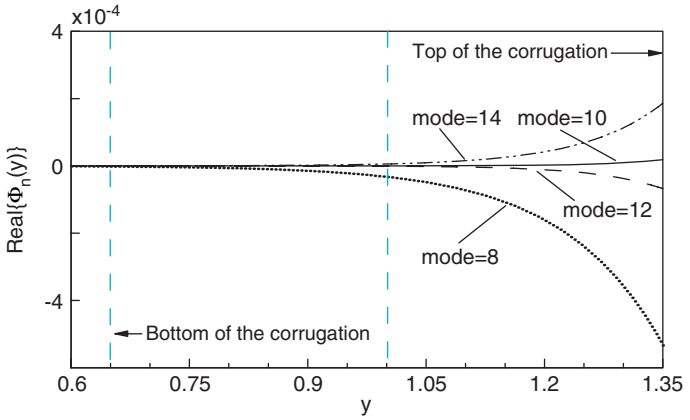

Figure 3. Distribution of the real part of the amplitude function $\Phi^{(n)}(y, t)$ as a function of y for $t \to \infty$ (steady state) for higher Fourier modes ($n \geqslant 8$) in the area close to the upper wall for the model problem (33) for $\alpha = 1.0$ and $S = 0.35$ (distance between the top and bottom of the corrugation $2S = 0.7$) determined using the IBC method with $N_M = 16$ Fourier modes and $N_T = 70$ Chebyshev polynomials.

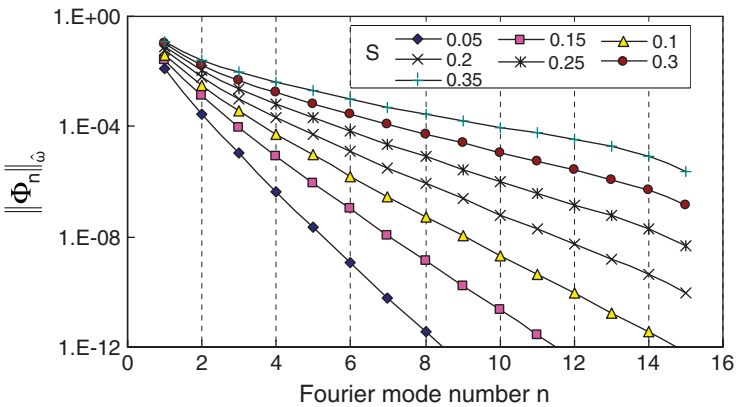

Figure 4. Variations of the Chebyshev norm (34) of the modal function $\Phi^{(n)}(y, t)$ for $t \to \infty$ (steady state) as a function of the Fourier mode number n for the model problem (33) for the corrugation wavenumber $\alpha = 1.0$ and for different amplitudes S of the corrugation determined using the IBC method with $N_M = 15$ Fourier modes and $N_T = 70$ Chebyshev polynomials.

to machine accuracy. Chebyshev norm defined as

$$\|\Phi^{(n)}\|_{\hat{\omega}} = \sqrt{\int_{-1}^{1} \Phi^{(n)}(\hat{y}, t)\Phi^{(n)*}(\hat{y}, t)\hat{\omega}(\hat{y})\,\mathrm{d}\hat{y}}, \quad \hat{\omega} = 1/\sqrt{1 - \hat{y}^2} \tag{34}$$

has been adopted as a measure of the 'magnitude' of the modal function $\Phi^{(n)}$. Results displayed in Figure 4 demonstrate that this norm decreases as a function of the mode number n with the rate of decrease very rapidly reaching the (asymptotic) exponential form.

DOI: 10.1002/fld

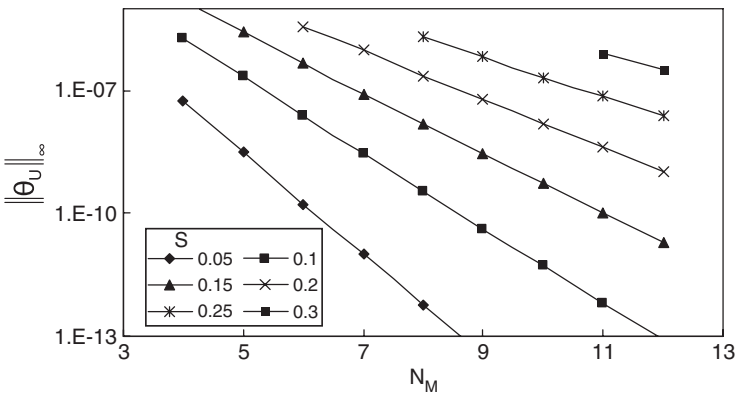

Figure 5. Variation in the $\|\theta_U(x,t)\|_\infty$ norm (see Equation (35)) as a function of the total number of Fourier modes N_M used in the computations for $t \to \infty$ (steady state) for the model problem (33) for the corrugation wavenumber $\alpha = 1.0$ and for different corrugation amplitudes S evaluated using the IBC method with $N_T = 70$ Chebyshev polynomials.

Accuracy of the enforcement of boundary conditions (8a) and (8b) is crucial for the immersed boundary conditions method. While the unknown θ should satisfy boundary conditions (4a) and (4b), only first N_M Fourier modes are set to zero. The rest of the available Fourier modes (for $N_M + 1 < n < N_\theta$) provides a suitable measure of the magnitude and spectral decomposition of the error. For convenience, we use the L_∞ norm for θ evaluated at the upper wall defined as

$$\|\theta_U(x,t)\|_\infty = \sup_{0 \leqslant x \leqslant 2\pi/\alpha} |\theta(x, y_U(x), t)| \tag{35}$$

to judge the performance of the method. This norm is very strict and thus provides an unambiguous way to judge the accuracy of the boundary conditions. Figure 5 displays variations of $\|\theta_U(x,t)\|_\infty$ as a function of the total number of Fourier modes N_M used in the calculations. It can be seen that the magnitude of contributions of higher modes to the complete solution decreases exponentially. Distribution of $\theta_U(x,t)$ over a single period is displayed in Figure 6. This function is oscillatory in x with the maximum occurring around $x = \pi/2$, i.e. around the top of the corrugation. The location of the maximum of the error is associated with the fact that the modal functions $\Phi^{(n)}$ reach maximum around the extremes of the solution domain (see Figure 3) and thus the contributions of the higher Fourier modes are relatively more important around the top of the corrugation; the rate of error reduction as a function of the total number of Fourier modes N_M is thus smaller in the vicinity of the top of the corrugation as compared with its top. This effect is more pronounced for higher values of α due to the fact that boundary layers in the distribution of $\Phi^{(n)}$ of sufficiently high index are thinner than the depth of the corrugation.

The implementation of boundary conditions (4a) and (4b) using the immersed boundary conditions method guarantees that the Fourier spectrum of θ_U should not contain harmonics of order lower than N_M. This property provides a test for accuracy and consistency of the method. Results shown in Figure 7 demonstrate that the first eight Fourier modes had been eliminated, as expected.

A series of tests had been carried out in order to check if the method produces any spurious spatial oscillations. Figure 8 illustrates results of a test for the wall with the corrugation wavenumber $\alpha = 3$ and the amplitude $S = 0.1$. In case A, the corrugation was assumed to have

DOI: 10.1002/fld

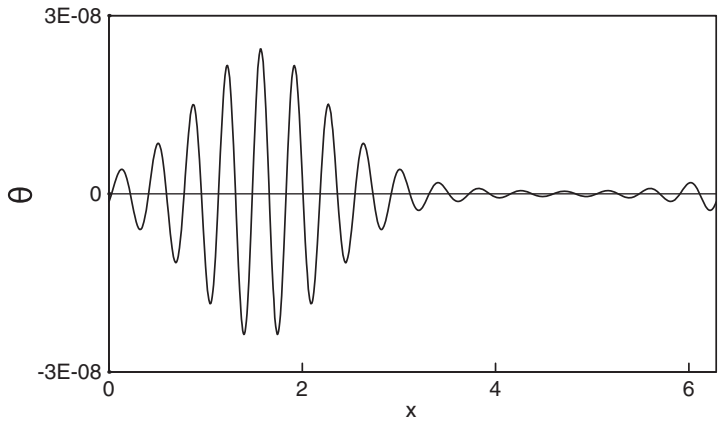

Figure 6. Distribution of θ evaluated at the upper wall for $t \to \infty$ (steady state) for the model problem (33) for the corrugation wavenumber $\alpha = 1.0$ and amplitude $S = 0.35$ evaluated using the IBC method with $N_M = 15$ Fourier modes and $N_T = 70$ Chebyshev polynomials.

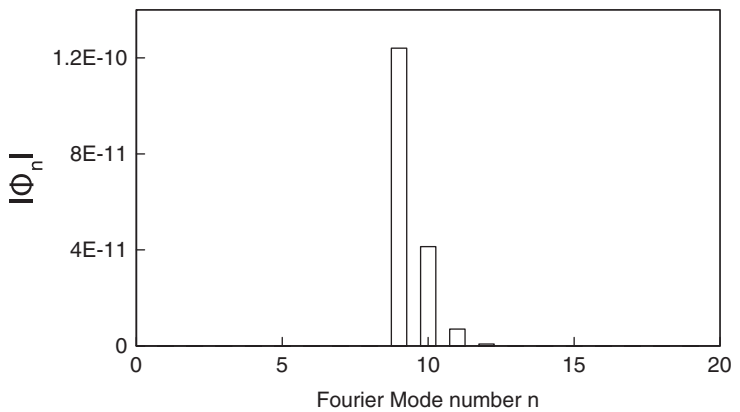

Figure 7. Fourier spectra of distribution of θ_U for $t \to \infty$ (steady state) for the model problem (33) with the corrugation amplitude $S = 0.1$ and the corrugation wavenumber $\alpha = 1.0$ evaluated using the IBC method with $N_M = 8$ Fourier modes and $N_T = 70$ Chebyshev polynomials.

the shape of the principal Fourier mode and the calculations had been carried out with $N_M = 6$ Fourier modes. In case B, the same shape was assumed to be represented by the second Fourier mode (the principal mode has the wavenumber $\alpha = 1.5$), while in case C it was represented by the third Fourier mode (the principal mode has the wavenumber $\alpha = 1$). In order to have fully equivalent representations, the number of Fourier modes used in cases B and C were $N_M = 12$ and 18, respectively. The selected representations admitted subharmonics of the $1/2$ type in case B and $1/3$ type in case C. The Fourier spectra shown in Figure 8 demonstrate the equivalency of the results in all three cases. No subharmonics had been produced during the solution process and the modes expected to produce zero contributions in cases B and C behaved as expected.

DOI: 10.1002/fld

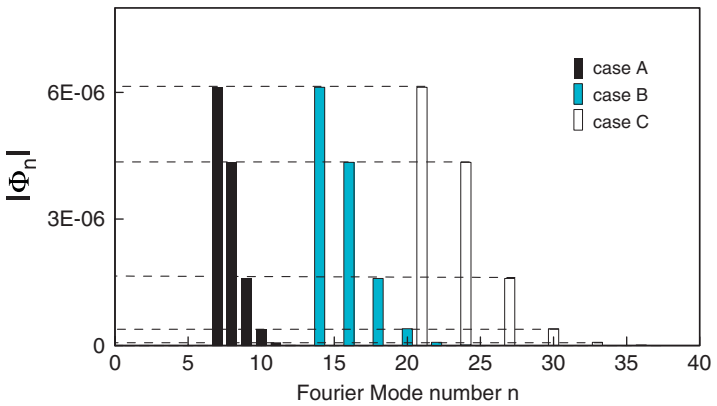

Figure 8. Fourier spectra of θ_U for $t \to \infty$ (steady state) for the model problem (33) with the corrugation amplitude $S = 0.1$ and the corrugation wavelength $\lambda = 2\pi/3$ determined using three different forms of Fourier expansions in the IBC method. Case A:$\alpha = 3.0$, $N_M = 6$; case B: $\alpha = 1.5$, $N_M = 12$ and case C: $\alpha = 1.0$, $N_M = 18$. $N_T = 70$ Chebyshev polynomials used in all cases.

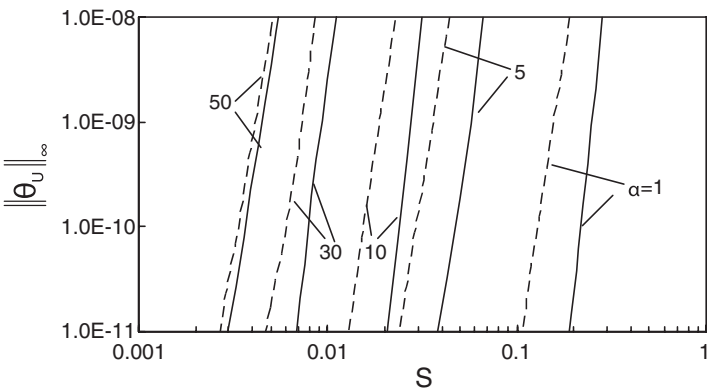

Figure 9. The $\|\theta_U(x,t)\|_\infty$ norm (see Equation (35)) evaluated for $t \to \infty$ (steady case) using the IBC method as a function of the corrugation amplitude S for selected values of the corrugation wavenumbers α for the model problem (33). The dashed and solid lines represent results obtained with the $N_M = 10$, 15 Fourier modes, respectively. The reader may note that $S = 2$ corresponds to the corrugation trough reaching the center of the slot. $N_T = 70$ Chebyshev polynomials used in the calculations.

Dependence of the boundary error as a function of geometric parameters, i.e. α and S, for a fixed number of Fourier modes N_M has been investigated. The norm $\|\theta_U(x,t)\|_\infty$ was used a measure of error. Figure 9 illustrates variations of this norm as a function of the corrugation amplitude S for selected values of the wavenumber α, and Figure 10 shows variations of this norm as a function of the wavenumber α for selected values of the amplitude S. The reader may note in judging these results that $S = 2$ corresponds to a situation when the bottom of the corrugation touches the lower wall. The available results suggest that the error is at machine accuracy level if α and S are below certain critical values. Once these values are reached, the error begins to increase rapidly

DOI: 10.1002/fld

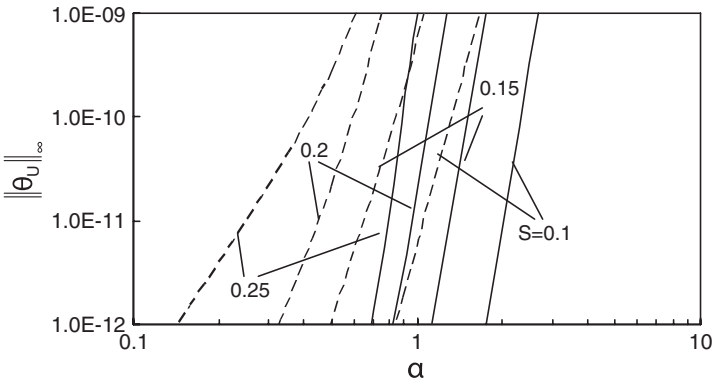

Figure 10. The $\|\theta_U(x,t)\|_\infty$ norm (see Equation (35)) evaluated for $t \to \infty$ (steady case) using the IBC method as a function of the corrugation wavenumber α for selected values of the corrugation amplitude S for the model problem (33). The dashed and solid lines represent results obtained with the $N_M = 10$, 15 Fourier modes, respectively. The reader may note that $S = 2$ corresponds to the corrugation trough reaching the center of the slot. $N_T = 70$ Chebyshev polynomials used in the calculations.

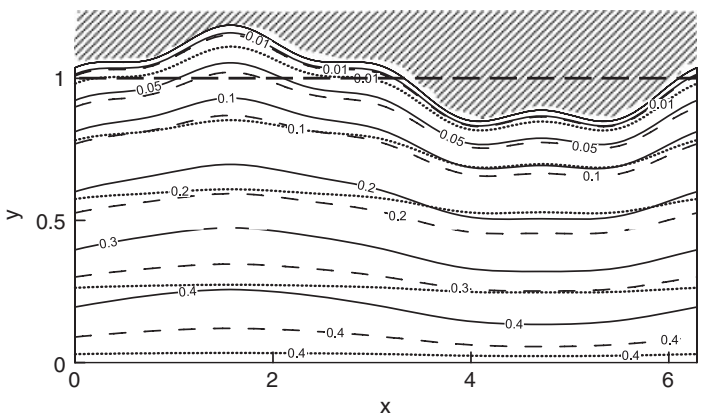

Figure 11. Instantaneous isotherms in the upper part of a slot bounded by $y_L(x,t) = -1$, $y_U(x,t) = 1 + (-0.075ie^{i\alpha x} + 0.01875ie^{4i\alpha x} + CC)$ at time $t = 0.5$ (dot lines), $t = 1.0$ (dash lines) and $t = \infty$ (solid lines) determined using both the IBC and the DT methods. Results obtained by both methods overlap.

in a fairly universal manner. These critical values of α and S can be increased by increasing the number of Fourier modes N_M used in the calculation, but the qualitative character of the error increase remains unchanged.

The above test had been carried out for a corrugation in the form of a single Fourier mode. The algorithm is general, however, and can deal with any corrugation shape that is represented by a Fourier expansion. Figure 11 shows instantaneous isotherms in a slot bounded by a smooth wall from below and wall with shape defined as $1 + (-0.075ie^{ix} + 0.01875e^{4ix} + CC)$ from above. Figure 12 shows instantaneous heat flux at the upper wall of the same slot.

DOI: 10.1002/fld

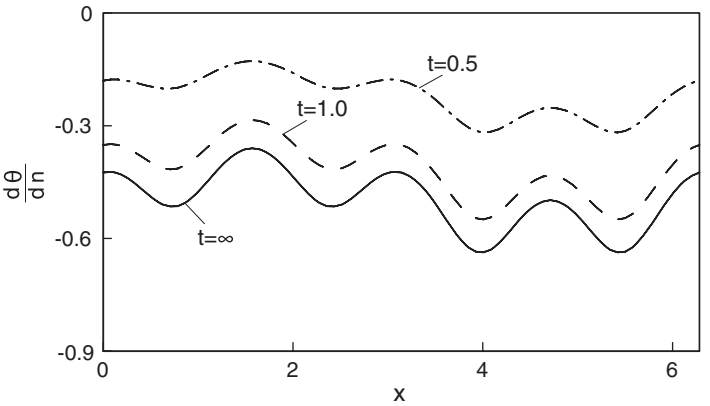

Figure 12. Instantaneous heat flux at the upper wall of the slot described in Figure 11 determined using the IBC and the DT methods with $N_M = 15$ Fourier modes and $N_T = 80$ Chebyshev polynomials. Results obtained using both methods overlap.

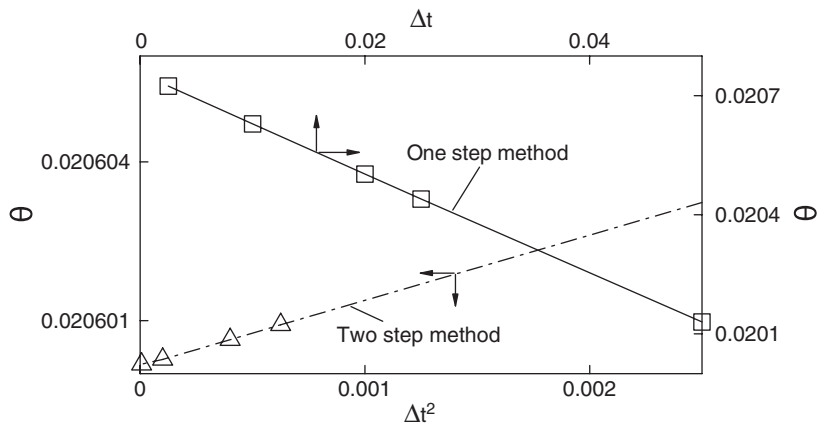

Figure 13. Variation in the dependent variable θ at a test point located at $x = \pi$, $y = 0.95$ in a slot bounded by $y_L(x,t) = -1$, $y_U(x,t) = 1 + (-0.05ie^{ix} + CC)$ at a time $t = 1$ as a function of the time-step size Δt evaluated using both methods (IBC and DT) with $N_M = 10$ Fourier modes and $N_T = 60$ Chebyshev polynomials. Results obtained by both methods overlap.

Tests discussed so far were focused on the analysis of error associated with the spatial discretization. The temporal discretization is second-order accurate for the two-step method and results of tests shown in Figure 13 demonstrate that this error is indeed second order when the boundary conditions are enforced using the immersed boundary conditions method. Similar tests for the one-step method described in Appendix A demonstrate the first-order accuracy (see Figure 13). The reader may note that the test problem has a steady solution as $t \to \infty$. This solution, which has been determined numerically using the steady version of the algorithm, agrees with the unsteady solution determined numerically after about five time units, providing further verification of the

DOI: 10.1002/fld

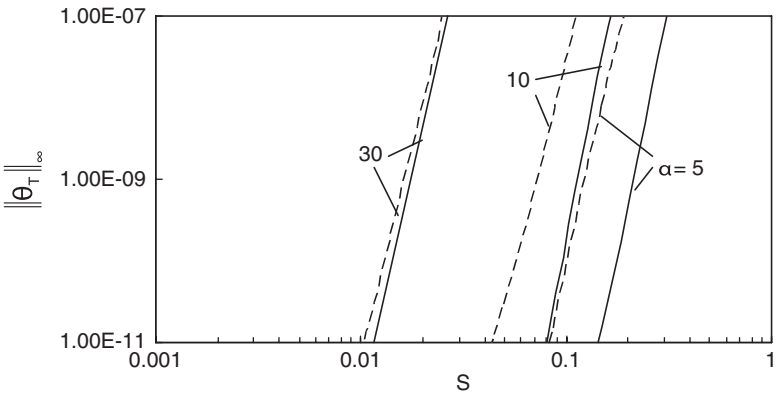

Figure 14. The norm $\|\theta_T(x,t)\|_\infty$ (see Equation (36)) evaluated for $t \to \infty$ using the DT method as a function of the corrugation amplitude S for selected values of the corrugation wavenumber α for the model problem (33). The tested values determined using $N_M = 10$ and 15 Fourier modes are shown using dashed and solid lines, respectively. The reference values have been determined using $N_M = 45$ Fourier modes. $N_T = 100$ Chebyshev polynomials were used in all calculations.

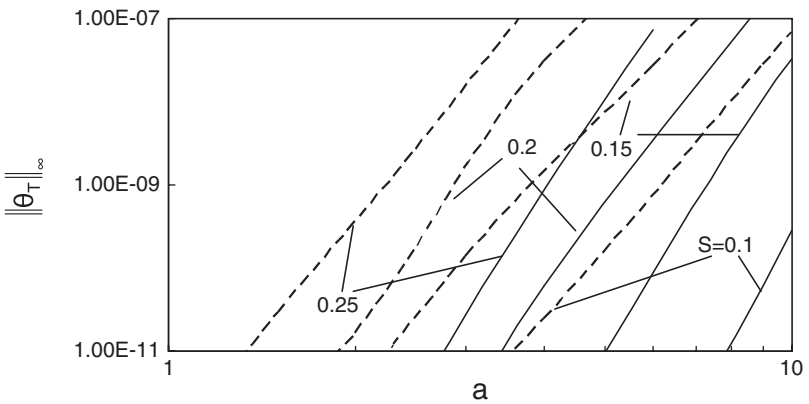

Figure 15. The norm $\|\theta_T(x,t)\|_\infty$ (see Equation (36)) evaluated for $t \to \infty$ using the DT method as a function of the corrugation wavenumber α for selected values of the corrugation amplitude S for the model problem (33). The tested values determined using $N_M = 10$ and 15 Fourier modes are shown using dashed and solid lines, respectively. All other conditions as in Figure 14.

performance of the algorithms. No numerical instability problems have been identified regardless of whether a direct or an iterative method of solution of the discretized equation was used.

5.2. *Domain transformation method*

While the algorithm described in Section 4 delivers spectral accuracy, it can be applied only in geometries that do not lead to singular and near singular mappings. In the case of test problem (33), the singular mapping occurs for $\alpha \to \infty$ and one should expect accuracy problems when α becomes too large. This problem is illustrated in Figure 14 showing variations in the error norm

DOI: 10.1002/fld

defined as

$$\|\theta_T(x,t)\|_\infty = \sup_{0\leqslant x\leqslant 2\pi/\alpha} |\theta(x, y_{\eta=0.95}, t)_{\text{com}} - \theta(x, y_{\eta=0.95}, t)_{\text{ref}}| \tag{36}$$

as a function of the corrugation amplitude S for selected values of the corrugation wavenumber α, and in Figure 15 as a function of the corrugation wavenumber α for a few selected values of the corrugation amplitude S. The reference solution θ_{ref} that is used for comparisons has been evaluated numerically using large number of Fourier modes and Chebyshev polynomials so that the errors associated with the truncations of the Fourier and Chebyshev expansions had been reduced below the round-off error. It can be seen that the error increases rapidly once a certain critical value of either the wavenumber α or the amplitude S has been reached. This error rise occurs, however, for the values of α and S that are larger than those for which a similar error rise occurred in the case of the IBC method (see Figures 9 and 10).

6. COMPARISON OF THE IBC AND DT METHODS

The IBC and DT methods can deal with a similar class of problems and thus one may inquire which method is 'better'. It is clear from the discussion in Sections 3 and 4 that the IBC method results in simpler equations and thus the programming effort is smaller. The computational efficiency requires a more detailed discussion. Results displayed in Figure 16 show that the DT method requires use of fewer Fourier modes in order to achieve the same level of error, and Figure 17 demonstrates that both methods indeed produce the same results. Table I illustrates computational effort required to produce a steady-state solution using both methods implemented with the same number of Fourier modes and Chebyshev polynomials. All tests had been done on the same hardware using Matlab as the computing environment. The computational effort in this case consists of construction of the coefficient matrix, inversion of this matrix and multiplication of the inverted matrix by the

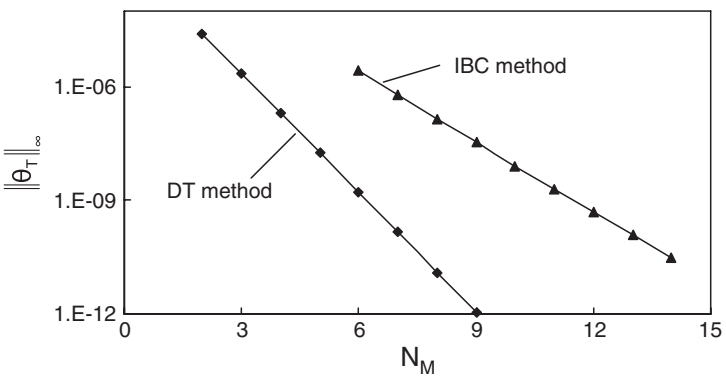

Figure 16. Variation in the norm $\|\theta_T(x,t)\|_\infty$ (see Equation (36)) for $t \to \infty$ evaluated using IBC and DT methods as a function of the number of Fourier modes N_M used in the calculations for the slot bounded by $y_L(x,t) = -1$ and $y_U(x,t) = 1 + (-0.1e^{ix} + CC)$. The reference quantity has been evaluated with $N_M = 20$ Fourier modes and $N_T = 70$ polynomials, while the test quantity has been evaluated with variables N_M and $N_T = 70$.

DOI: 10.1002/fld

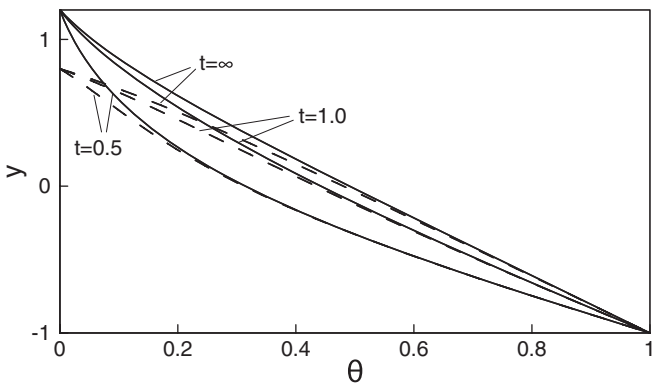

Figure 17. Instantaneous temperature profiles at the x-locations corresponding to the widest (solid lines) and narrowest (dotted lines) opening of a slot bounded by $y_L(x,t) = -1$, $y_U(x,t) = 1 + (-0.175ie^{3ix} + CC)$ determined using the IBC and DT methods with $N_M = 15$ Fourier modes and $N_T = 70$ Chebyshev polynomials. Results obtained by both methods overlap.

Table I. Comparison of computational times required for the evaluation of the steady-state solution in the case of test problem (33) with the corrugation wavenumber $\alpha = 1$ and the corrugation amplitude $S = 0.2$.

Number of Fourier modes (N_M)	IBC method			DT method		
	Time required (in s) for			Time required (in s) for		
	Matrix construction	Matrix inversion	Matrix multiplication	Matrix multiplication	Matrix inversion	Matrix multiplication
10	2.5572	6.5694	0.0170	266.5011	6.6357	0.0184
15	8.0496	20.1827	0.0458	592.8096	20.3958	0.0365

Note: Times for different elements of the IBC and DT methods implemented with the same number N_M of Fourier modes produced using $N_T = 70$ Chebyshev polynomials are given.

right-hand side. The reader may note a significantly higher computational cost of construction of the coefficient matrix in the case of the DT method. Since the DT method requires fewer Fourier modes to produce the same level of accuracy, as demonstrated in Figure 16, one may inquire if this could improve the relative performance of this method. Results provided in Table II demonstrate that the IBC method is still more efficient in spite of the using a larger number of Fourier modes.

The relative performance of both methods in the case of unsteady simulations can be deduced from Tables I and II. The additional computational effort as compared with the steady-state case involves one multiplication of the inverted matrix per time step. The DT method could overcome its initial handicap associated with matrix construction if simulations are to be carried out over a very long time using constant time step, as the cost of its matrix multiplication is lower than in the IBC method. In the case of a variable time step, the coefficient matrix needs to be reconstructed at each time step and then the IBC method becomes significantly more efficient.

We shall now consider potential gains in the efficiency of the IBC method when the direct solution discussed above is replaced by the decoupled algorithm. Results of tests in the case of

DOI: 10.1002/fld

Table II. Comparison of computational time requirements for different elements of the IBC and DT methods necessary to produce steady-state solution with a desired accuracy (as measured by norm (36)).

	IBC method				DT method			
	Required number of	Time required (in s) for			Required number of	Time required (in s) for		
Desired accuracy	of Fourier modes N_M	Matrix construction	Matrix inversion	Matrix multiplication	Fourier modes N_M	Matrix multiplication	Matrix inversion	Matrix multiplication
10^{-6}	6	0.6721	1.7338	0.0053	3	28.3172	0.3044	0.0021
10^{-8}	10	2.6013	6.5894	0.0127	5	71.5123	1.0716	0.0050
10^{-10}	13	5.3527	13.5591	0.0197	7	134.6521	2.5360	0.0088

Note: Other test conditions as in Table I.

steady solution are illustrated in Table III. The decoupled algorithm is significantly faster for the whole range of roughness amplitudes for which convergence can be achieved. The solution oscillates in the case of the most extreme conditions considered in Table III, but does not diverge. One may note an increase in the number of required iterations as the amplitude of the corrugation increases.

The relative performance of the direct- and mode-decoupled algorithms in the unsteady case is illustrated in Table IV. Since the overall accuracy of the simulations is determined by the error of the temporal discretization, the convergence criterion for the decoupled algorithm in these tests had been set at 10^{-5}. The cost of using the mode-decoupled algorithm is generally similar to the cost of the direct algorithm in spite of the fact that a complete solution has to be produced at each time step in the former case and only a single matrix multiplication is required in the latter case. The direct algorithm should be faster if long-time simulations with constant time step are required. This advantage is lost in the case of a variable time step when the decoupled algorithm is much more efficient due to the cost of matrix construction and inversion in the direct algorithm.

The performance of the decoupled algorithm can be improved by taking advantage of the information available in the previous time step and re-arranging the iteration strategy. Three different strategies have been tested and the results are displayed in Table V. Version A is exactly the same as in the case of steady solution, version B uses extrapolated values of the modal functions during the first iteration and version C uses only extrapolated values of the modal functions and eliminates iterations. In all cases, the method remains second-order accurate as the extrapolation provides second-order accuracy in time. The results (see Table V) show significant improvements of performance of versions B and C over version A but only when the corrugation amplitude is not too large. Version C is least resistant to the increase in the amplitude and it diverges at certain critical value of S (which depends on the corrugation wavenumber). Version B can work with amplitudes S twice as big as in version C, but its performance rapidly deteriorates and becomes worse than version A as corrugation amplitude increases. Version A also diverges but at the amplitude levels comparable to those where the accuracy of the IBC algorithm becomes questionable (see Figures 9 and 10).

The above results show that the decoupled IBC algorithm is generally more efficient than the direct algorithm. This algorithm would also be favored because of the reduced memory use and potential gains offered by parallelization. No attempt was made as a part of this work to measure gains associated with the last two effects.

DOI: 10.1002/fld

Table III. Variations in time requirements for the direct and decoupled IBC algorithms in the case of steady-state solution determined with the predetermined accuracy (measured by norm (36)) as a function of the corrugation amplitude S for the model problem (33) with the corrugation wavenumber $\alpha = 1.0$ determined using $N_T = 70$ Chebyshev polynomials.

		Direct IBC method				Iterative IBC method		
			Time required (in s) for					
S	Desired accuracy	Required N_M	Matrix construction	Matrix inversion	Matrix multiplication	Required N_M	Number of iterations required	Total time required (in s) to solve
0.05	10^{-6}	3	0.1162	0.3065	0.0014	3	3	0.0742
	10^{-8}	5	0.3947	1.1330	0.0034	5	4	0.0920
	10^{-10}	7	0.9990	2.5726	0.0068	7	5	0.1183
0.1	10^{-6}	4	0.2345	0.6341	0.0024	4	4	0.0823
	10^{-8}	6	0.6498	1.7159	0.0047	6	6	0.1207
	10^{-10}	9	1.9178	5.0107	0.0098	9	8	0.1816
0.15	10^{-6}	5	0.4077	1.1445	0.0039	5	5	0.1023
	10^{-8}	8	1.4427	3.6312	0.0087	8	9	0.1753
	10^{-10}	11	3.3894	8.5863	0.0148	11	18	0.4367
0.2	10^{-6}	6	0.6721	1.7338	0.0053	6	6	0.1205
	10^{-8}	10	2.6013	6.5894	0.0127	10	23	0.4947
	10^{-10}	13	5.3527	13.5591	0.0197	13	63	1.7762
0.25	10^{-6}	10	2.5966	6.7209	0.0127	10	12	0.2684
	10^{-8}	13	5.3632	13.7868	0.0206	13	97	2.5722
	10^{-10}	17	11.5617	29.0973	0.0342	17	476	17.5857
0.3	10^{-6}	12	4.3526	11.0597	0.0169	12	31	0.8163
	10^{-8}	17	11.5587	29.1068	0.0337	17	737	27.8263
	10^{-10}	21	21.2536	53.0861	0.0504	Cannot achieve desired accuracy		

Note: Other test conditions as in Table I.

Table IV. Comparison of time requirements associated with the direct and decoupled algorithms implemented with the same number of Fourier modes in the IBC method.

	Direct IBC method			Iterative IBC method
	Time required (in s) for			
Number of Fourier modes (N_M)	Matrix construction	Matrix inversion	Matrix multiplication for 100 time steps	Time required for simulation over 100 time steps
10	2.5398	6.5706	2.7452	5.0152
15	8.0331	20.3538	5.1756	96.5563

Note: The two-step method with the time step $\Delta t = 0.01$ was used with the convergence criterion for the iterative solution set at 10^{-5}. Other test conditions as in Table I.

DOI: 10.1002/fld

Table V. Comparison of time requirements of different decoupling schemes for the IBC method as a function of the corrugation amplitude S with the corrugation wavenumber $\alpha = 1.0$.

Corrugation amplitude, S	Total time required for 100 time steps (in s)		
	Version A	Version B	Version C
0.05	11.6123	5.4772	5.3845
0.10	23.6266	6.3542	4.8706
0.15	44.6777	31.8473	Diverges
0.20	96.5563	256.4365	Diverges
0.25	578.3254	Diverges	Diverges
0.30	Diverges	Diverges	Diverges

Note: Calculations have been carried out with $N_M = 15$ Fourier modes and $N_T = 70$ Chebyshev polynomials. Version A—complete iterations, version B—complete iterations coupled with extrapolation for the first iteration, version C—extrapolation with no iterations. Other test conditions as in Table IV.

7. CONCLUSION

An immersed boundary conditions method was developed for unsteady flow problems in irregular, corrugated geometries governed by the Laplace operator. The method uses a fixed computational domain with boundaries of the flow domain submerged inside the computational domain. The problem formulation is closed by replacing boundary conditions normally applied at the ends of the computational domain with constraints enforced along the boundaries of the flow domain. One- and two-step implicit methods have been developed. It has been demonstrated that the algorithm delivers spectral accuracy for the spatial discretization and the first- and second-order accuracies for the temporal discretization in the case of the one- and two-step methods, respectively. The error of spatial discretization grows rapidly when the wavenumber and the amplitude that characterize corrugation grow beyond certain critical level. The efficiency of the algorithm has been judged by comparing it with the classical algorithm based on the domain transformation. The immersed boundary conditions method results in less programming effort and is generally more efficient computationally when compared with the domain transformation method. It has been shown that the performance of the immersed boundary conditions method can be further improved by using an iterative solution based on mode decoupling (mode-decoupled algorithm) rather than the direct solution. Three versions of this algorithm have been considered with the most efficient one limited to small corrugation amplitudes and the least efficient one having the range of applications similar to that found in the case of the direct solution. In all cases, mode-decoupled algorithm was found to be more efficient than the direct algorithm. This algorithm also offers potential for efficiency gains through parallelization of the computations and through significant reduction of memory use.

APPENDIX A

Temporal discretization of (10) using a one-step implicit method results in

$$[\Gamma^2 D^2 - (n^2\alpha^2 + \Delta t^{-1})]\Phi_{\tau+1}^{(n)} = -\Delta t^{-1}\Phi_{\tau}^{(n)}, \quad n \in \langle 0, N_M \rangle$$

DOI: 10.1002/fld

Temporal discretization of (25) using the same method results in

$$D^2\Psi^{(n)}_{\tau+1} + \sum_{s=-N_M}^{N_M} [w_1^{(n-s)} + \mathrm{i}s\alpha w_2^{(n-s)}]D\Psi^{(s)}_{\tau+1} - \sum_{s=-N_M}^{N_M} [(s\alpha)^2 + \Delta t^{-1}]w_3^{(n-s)}\Psi^{(s)}_{\tau+1}$$

$$= -\Delta t^{-1} \sum_{s=-N_M}^{N_M} w_3^{(n-s)}\Psi^{(s)}_{\tau}, \quad n \in \langle 0, N_M \rangle$$

APPENDIX B

Expressions required in Equation (25):

$$\eta_x = [(y_L)_\xi(\eta - 1) - (y_U)_\xi(\eta + 1)]/(y_U - y_L)$$

$$\eta_{xx} = \frac{\eta(y_U - y_L)[(y_L)_\xi - (y_U)_\xi][(y_L)_{\xi\xi} - (y_U)_{\xi\xi}] + 2y_L(y_U)_{\xi\xi} - 2y_U(y_L)_{\xi\xi}}{(y_U - y_L)^2}$$

$$+ \frac{-2\eta[(y_U)_\xi - (y_L)_\xi]^2 + 2[(y_U)_\xi^2 - (y_L)_\xi^2]}{(y_U - y_L)^2}$$

$$\eta_y = \frac{2}{y_U - y_L}$$

where the subscript ξ denotes derivative $\mathrm{d}/\mathrm{d}\xi$.

ACKNOWLEDGEMENTS

This work has been carried out with support from SHARCNET and NSERC of Canada. SHARCNET of Canada provided the computing resources.

REFERENCES

1. Peskin CS. The fluid dynamics of heart valves: experimental, theoretical and computational methods. *Annual Review of Fluid Mechanics* 1981; **14**:235–259.
2. Mittal R, Iaccarino G. Immersed boundary methods. *Annual Review of Fluid Mechanics* 2005; **37**:239–261.
3. Floryan JM, Rasmussen H. Numerical analysis of viscous flows with free surfaces. *Applied Mechanics Reviews* 1989; **42**:323–341.
4. Szumbarski J, Floryan JM. A direct spectral method for determination of flows over corrugated boundaries. *Journal of Computational Physics* 1999; **153**:378–402.

DOI: 10.1002/fld